Mn^{5+} Lifetime-Based Thermal Imaging in the Optical Transparency Windows Through Skin-Mimicking Tissue Phantom

Wojciech M. Piotrowski,* Riccardo Marin, Maja Szymczak, Emma Martín Rodríguez, Dirk H. Ortgies, Paloma Rodríguez-Sevilla, Miroslav D. Dramićanin, Daniel Jaque, and Lukasz Marciniak*

Lifetime-based luminescence thermometry has been shown to enable accurate deep-tissue monitoring of temperature changes – even at the in vivo level – in a minimally invasive way. However, major limiting factors to the performance of this approach are short lifetimes and poor brightness. These are characteristics, respectively, of semiconductor nanocrystals and lanthanide-doped nanoparticles, of which most luminescent nanothermometers are made. To address these limitations, the composition of luminescent nanothermometers co-doped with transition metal (Mn^{5+}) and Er^{3+} ions are designed and optimized. The salient features of these nanothermometers are strong, near-infrared emission and long, temperature-dependent photoluminescence lifetime. The potential of these luminescent nanophosphors for thermal sensing is then showcased by monitoring a thermal gradient using a one-of-a-kind piece of equipment designed for lifetime-based luminescence thermometry measurements. The combination of the newly developed nanothermometers and the custom-made instrument allows for obtaining 2D thermal maps both in the absence and presence of tissue phantoms mimicking the optical properties of the skin. The results presented in this study thus provide credible foundations for the deployment of lifetime-based thermometry for accurate deep-tissue thermal mapping at the preclinical level.

1. Introduction

Temperature measurement in biological systems is an extremely valuable source of information about the onset of diseases and inflammation events, as well as the biological processes associated with their course.[1] On the other hand, real-time thermal monitoring is essential for targeted therapies, e.g. light-induced hyperthermia, where accurate in situ temperature sensing can significantly reduce the undesirable side effects related to overheating of healthy cells and tissues.[2–6] Nevertheless, classical approaches for temperature readout are not suitable for the above-mentioned applications because the contact manner of temperature readout is too invasive, and most of them provide only information about the local temperature, preventing temperature imaging.[7,8] Thermographic infrared cameras can afford noninvasive and remote temperature measurement but their response

W. M. Piotrowski, M. Szymczak, L. Marciniak
Institute of Low Temperature and Structure Research
Polish Academy of Sciences
Okólna 2, Wroclaw 50–422, Poland
E-mail: w.piotrowski@intibs.pl; l.marciniak@intibs.pl
R. Marin, D. H. Ortgies, P. Rodríguez-Sevilla, D. Jaque
Nanomaterials for Bioimaging Group (nanoBIG)
Materials Physics Department
Facultad de Ciencias
Autonomous University of Madrid
C/ Francisco Tomás y Valiente 7, Madrid 28049, Spain

E. Martín Rodríguez
Nanomaterials for Bioimaging Group (nanoBIG)
Department of Applied Physics
Facultad de Ciencias
Autonomous University of Madrid
C/ Francisco Tomás y Valiente 7, Madrid 28049, Spain
E. Martín Rodríguez, D. H. Ortgies, P. Rodríguez-Sevilla, D. Jaque
Nanomaterials for Bioimaging Group (nanoBIG)
Instituto Ramón y Cajal de Investigación Sanitaria (IRYCIS)
Hospital Ramón y Cajal
Ctra. De Colmenar Viejo km 9.100, Madrid 28034, Spain
M. D. Dramićanin
Centre of Excellence for Photoconversion
Vinča Institute of Nuclear Sciences – National Institute
of the Republic of Serbia
University of Belgrade
P.O. Box 522, Belgrade 11001, Serbia

**ADVANCED
SCIENCE NEWS**

www.advancedsciencenews.com

**ADVANCED
OPTICAL
MATERIALS**

www.advopticalmat.de

is limited to the tissue's surface, which precludes deep tissue thermal imaging with this method.[8–10] Moreover, to correctly determine the temperature, thermal cameras require information about the emissivity of the object. In the case of biological systems, this parameter depends on the type of tissue and may vary with time, which additionally affects the measurement reliability.

One of the biggest challenges of thermal imaging based on luminescence thermometry is to efficiently excite the phosphor (acting as a thermal probe) and receive the signal (the emitted photons) through the tissues of living organisms while maintaining the reliability of the thermal readout despite tissue-induced spectral distortions.[1,11–18] To this end, a luminescent thermometer being considered for biomedical applications should meet very stringent optical requirements, such as high brightness along with photon absorption and emission capabilities in the near-infrared (NIR) spectral range of the optical transparency windows (NIR-I: 680–950 nm, NIR-II: 1000–1350 nm, NIR-III: 1500–1800 nm).[19–23] Reduced attenuation of the optical signal in these spectral ranges facilitates deep-tissue thermal imaging. Although in luminescence thermometry the ratiometric approach – whereby the ratio between different integrated signals is used as thermometric parameter – is arguably the most common, its application in biomedical thermal imaging may lead to erroneous temperature readout.[11,24] This is because of the dispersive character of the photon extinction by the biological tissues, which may modify the shape of the emission spectra and thus affect the thermometric parameter. Therefore, the lifetime-based approach, which is negligibly affected by the photon-tissue interactions, is a promising alternative for deep-tissue thermal imaging.[25]

However, when considering this method, an additional requirement is necessary for phosphors to achieve satisfactory temperature resolution, namely relatively long lifetimes (optimally above the order of tens of microseconds) with a strong dependence on the temperature in the biological temperature range (293 – 333 K). Long lifetimes are ideal since the autofluorescence from tissue components is short-lived (nanoseconds).[26–28] Therefore, the precision and accuracy of lifetime-based thermometry are increased by selecting longer time gates where no contribution from the autofluorescence is present. Phosphors doped with transition metal (TM) ions can offer the ideal platform for this type of approach.[29]

TM ions are characterized by an absorption cross section significantly larger than the one of lanthanide ions (the other luminescent metal centers generally employed in luminescence thermometry).[30,31] Due to their 3d electronic configuration and crossover points between their energy levels parabolas, TM ions feature optical properties that are highly susceptible to temperature changes. Moreover, the spectroscopic properties of TMs can be modified by the crystal field strength.[29,30] Therefore, the spectral and thermometric parameters of the temperature probe based on TM can be modified by the change of the host material composition.[29]

Among TM ions, as recently shown by Ristic et al., Mn^{5+} ions meet all the criteria for a robust temperature probe.[32,33] Despite the expected influence of the crystal field on its spectroscopic properties, some of its absorption bands are located within NIR-I, which allows Mn^{5+} ions to be efficiently excited

through tissues.[33,34] Moreover, its narrow (full width at half maximum, FWHM < 5 nm) and intense emission associated with the $^1E \rightarrow {}^3A_2$ transition from the host materials studied so far is located in the 1100 – 1200 nm range, which ideally falls within NIR-II[32].[33] The main limitation of Mn^{5+} is the need to select a host material that allows the stabilization of the manganese ions at the 5+ oxidation state. According to Shannon,[35] Mn^{5+} exists only in a tetrahedral configuration, and its effective ionic radius is relatively small (33 pm). Therefore, it was assumed that one among the limited number of possibilities for effective substitution with Mn^{5+} ions would be the $(VO_4)^{3-}$ site in $Ba_3(VO_4)_2$.[36] In that study, an emission maximum at 1181 nm and FWHM = 3 nm under 592 nm excitation at room temperature and a long lifetime of 0.43 ms were presented. These promising features are the basis for further research on the luminescence of Mn^{5+} ions in this host material.

In this work, we report, to the best of our knowledge, the first instance of the temperature dependence of the excited level lifetimes of Mn^{5+} ions in $Ba_3(VO_4)_2$. A detailed structural and luminescence characterization study is presented, which aims to optimize the concentration of Mn^{5+} ions to obtain a highly sensitive luminescent thermometer based on the lifetimes of Mn^{5+} ions. Then, the effect of co-doping with selected lanthanide ions (Ln^{3+}) is investigated, as well as the effect of the concentration on the thermal evolution of the lifetimes of Mn^{5+} ions. Finally, a proof-of-concept experiment is conducted that exploits the thermometric dependence of Mn^{5+} lifetimes for thermal imaging of a sample with a temperature gradient, placed under a glass slide and under a skin-mimicking tissue phantom.

2. Experimental Section

The $Ba_3(VO_4)_2$:x% Mn^{5+} (x = 0.1; 0.2; 0.5; 1; 2; 5) and $Ba_3(VO_4)_2$:1% Mn^{5+}, y% Er^{3+} (y = 0.1; 0.2; 0.5; 1; 2) nanocrystals were synthesized with a modified Pechini method.[37] The following starting materials were used as reagents without further purification: $Ba(NO_3)_2$ (99.999%, Alfa Aesar), NH_4VO_3 (99.999% purity, Alfa Aesar), $MnCl_2 \cdot 4H_2O$ (>99.0%, Sigma Aldrich), Er_2O_3 (99.99%, Stanford Materials Corporation) and citric acid $HOC(CO_2H)(CH_2CO_2H)_2$ (>99.5%, Alfa Aesar). The starting materials were weighed so that the total amount of moles of metals was equal to $4.00 \cdot 10^{-4}$ mol. Stoichiometric amounts of $Ba(NO_3)_2$, NH_4VO_3 and $MnCl_2 \cdot 4H_2O$ were dissolved in deionized water in separate glasses and then mixed together. Erbium oxide was dissolved in deionized water with the addition of 2 mL of HNO_3 (65% purity, Avantor), then recrystallized three times to remove the excess nitrogen and added to the water solution of other reagents. After that, $24.0 \cdot 10^{-4}$ mol of anhydrous citric acid were added to a mixture with the molar ratio of citric acid to all metals set at 6:1. Next, the samples with x% Mn^{5+} concentration in respect to the number of V^{5+} ions and y% Er^{3+} in respect to the number of Ba^{2+} ions were calcined in porcelain crucibles at 1000 °C in the air for 8 h. Finally, the powders obtained were ground in an agate mortar.

All of the synthesized materials were examined by X-ray powder diffraction (XRPD) measurements carried out on PANalitycal X'Pert diffractometer, equipped with an Anton Paar

TCU 1000 N temperature control unit, using Ni-filtered Cu-K$_\alpha$ radiation (V = 40 kV, I = 30 mA). The Rietveld refinements were performed using the X'Pert HighScore Plus version 2.2.4 software.

Transmission electron microscope (TEM) images were taken using a FEI TECNAI G2 X-TWIN microscope. Powders were dispersed in methanol with the aid of ultrasounds and deposited on lacey-type copper grids. The studies were performed with 300 keV parallel beam electron energy. Images were digitally recorded using a Gatan Ultrascan 1000XP.

The emission spectra were measured using the 668 nm excitation lines from a laser diode and a NIRQUEST spectrometer from Ocean Optics (1.5 nm spectral resolution) as a detector. The excitation spectra and luminescence decay profiles were recorded using the FLS1000 Fluorescence spectrometer from Edinburgh Instruments with a R928P side window photomultiplier tube from Hamamatsu as a detector with a 450 W halogen lamp and 668 nm pulsed work laser diode as excitation sources. The low-temperature emission spectra were also obtained using the FLS1000 Fluorescence spectrometer. The temperature of the sample was controlled using a THMS 600 heating-cooling stage from Linkam (0.1 K temperature stability and 0.1 K set point resolution).

Tissue phantoms were prepared on a modified procedure given in.[38] For this purpose, different volumes of Intralipids (20% emulsion, Sigma Aldrich) were introduced into a 100 mL Erlenmeyer flask and water was added to reach a final volume of 50 mL. Phantoms, with 10, 25, 50, and 100% of Intralipids relative content were prepared. The mixture was introduced into an oil bath preheated at 363 K and kept under stirring (350 rpm). For tissue phantoms with Indian ink, 0.05, 0.1, or 0.2 wt.% of ink was added to the mixture at this stage. Next, 2 wt.% of agar powder was added and left with heating and stirring for 30 min until the agar was completely dissolved. After this time, the mixture was poured into a 1.3 mm thick crystallizing dish and allowed to cool to room temperature until the gel was set. All gels of 1.3 mm in thickness were stored in the fridge for further use.

For imaging experiments, the sample was placed in an optical setup specially designed for fluorescence imaging in the NIR-II, the PhotonSWIR Imager from BioSpace Lab (Nesles-la-Vallée, France). An InGaAs CCD camera (WiDy SenS 640V-ST, New Imaging Technologies, France) with a long pass filter at 1000 nm (Thorlabs FEL1000) and a fiber-coupled 808 nm laser diode (LIMO) were the principal components. For the first experiment without the presence of tissue phantom, the laser was set to a maximum output power of 14.1 mW and collected by a lens for illumination of the samples with a max (peak) power density of 0.052 mW cm^{-2} and an average power density of 0.026 mW cm^{-2}. For measurements via phantom tissue, the maximum output power of the laser was set to 2086 mW, resulting in a maximum power density of 215 mW cm^{-2} and an average power density of 61 mW cm^{-2}. The system was operated in pulsed mode with 10 ms pulses (resulting energy is 0.06 J) and a pulse-to-pulse separation of 35 ms (pulse repetition rate is 28 Hz). A time delay between the end of the laser pulse and camera acquisition was set to 20 μs at the beginning of the acquisition sequence. Then it is increased by 5 μs between each picture (exposure time 3.0 ms) and a series of 600 pictures were obtained, resulting in a final delay of 3.02 ms.

3. Results and Discussion

3.1. Structural and Morphological Characterization

Ba$_3$(VO$_4$)$_2$ crystallizes in a rhombohedral system of the R-$3m$ (166) space group. It is composed of [Ba$_{(1)}$(VO$_4$)$_2$]$^{4-}$ layers linked into a crystal network by Ba$_{(2)}$$^{2+}$ cations [39] (**Figure 1**a). Intra-layer Ba$_{(1)}$$^{2+}$ cations in this structure occupy D_{3d} symmetry sites that can be described as 6-fold coordinated octahedra. The metal-ligand distances between Ba$_{(1)}$$^{2+}$ ions and all surrounding O^{2-} ions are equal with the value of R(Ba$_{(1)}$$^{2+}$-O^{2-}) = 2.77831(2) Å. On the other hand, the interlayer Ba$_{(2)}$$^{2+}$ ions are located in the 10-fold coordinated sites with C_{3v} symmetry. In this case, the metal-ligand distances are as follows: six of them equal R$_1$(Ba$_{(2)}$$^{2+}$-O^{2-}) = 2.94654(4) Å, three R$_2$(Ba$_{(2)}$$^{2+}$-O^{2-}) = 2.78446(1) Å and one R$_3$(Ba$_{(2)}$$^{2+}$-O^{2-}) = 2.61609(2) Å. A single bond of the shortest length connecting Ba$_{(2)}$$^{2+}$ ions to the O^{2-} ion is shared with V^{5+} ions. For this reason, the VO$_4$$^{3-}$ groups in barium orthovanadate with C_{3v} symmetry are only slightly distorted from the tetrahedral geometry[39] with three R$_1$(V^{5+}-O^{2-}) = 1.73438(3) Å and one R$_2$(V^{5+}-O^{2-}) = 1.69715(1) Å. To understand which crystallographic positions can be replaced by the dopant ions, it is necessary to consider the effective ionic radii of the ions forming the host material, as well as those of the dopants. In the case of Ba$_3$(VO$_4$)$_2$, it is important to note the significant difference between the oxidation states (Ba^{2+} and V^{5+}), as well as the size of the ions: for 8-fold coordinated Ba^{2+} the effective ion radius (EIR) is 142 pm, for 10-fold coordinated Ba^{2+} the EIR equals 152 pm, whereas for V^{5+} located in the tetrahedron the EIR is equal to only 35.5 pm. Despite such a large difference between the ionic radii, when doping with manganese ions, three oxidation states (Mn^{2+}, Mn^{4+}, Mn^{5+}) could be considered depending on the crystallographic position that they may occupy. First, it is possible to consider the presence of 8-fold coordinated Mn^{2+} with EIR = 96 pm or 4-fold coordinated Mn^{5+} with EIR = 33 pm. It can be noted that in both cases, these ions have the same electric charge as the ions they can substitute (Ba^{2+} and V^{5+}, respectively). Estimating which of the proposed oxidation states will be more likely is possible by comparing the so-called misfit factor, which for Mn^{2+} is EIR$_{Mn2+}$^{VIII}/EIR$_{Ba2+}$^{VIII} = 96 pm/142 pm ≈0.68, compared to EIR$_{Mn5+}$^{IV}/EIR$_{V5+}$^{IV} = 33 pm/35.5 pm ≈0.93 for Mn^{5+} ions. The misfit factor should aim for 1.00, but highly probable doping can be assumed when the misfit factor is between 0.90 and 1.10. Hence the V^{5+} site is expected to be preferentially occupied by Mn^{5+} ions. Furthermore, the presence of Mn^{5+} ions was subsequently confirmed by spectroscopic measurements, while the emission of Mn^{2+} ions was not observed. On the other hand, it is also possible to consider 4-fold coordinated Mn^{4+} with EIR = 39 pm, due to the known high thermodynamic stability of Mn^{4+} ions. The misfit factor, in this case, is EIR$_{Mn4+}$^{IV}/EIR$_{V5+}$^{IV} = 39 pm/35.5 pm ≈1.10, which is a value in a similar deviation from 1.00 as in the case of Mn^{5+}. Nevertheless, in this case, there would be a charge mismatch, which would generate additional oxygen vacancies in the host material, which is energetically unfavorable. Furthermore, Mn^{4+} is highly energetically favorable at octahedral sites and known for its bright red emission, but in the case of Mn^{4+} ions at tetrahedral sites, the ions are not luminescent. This is in agreement with the work of
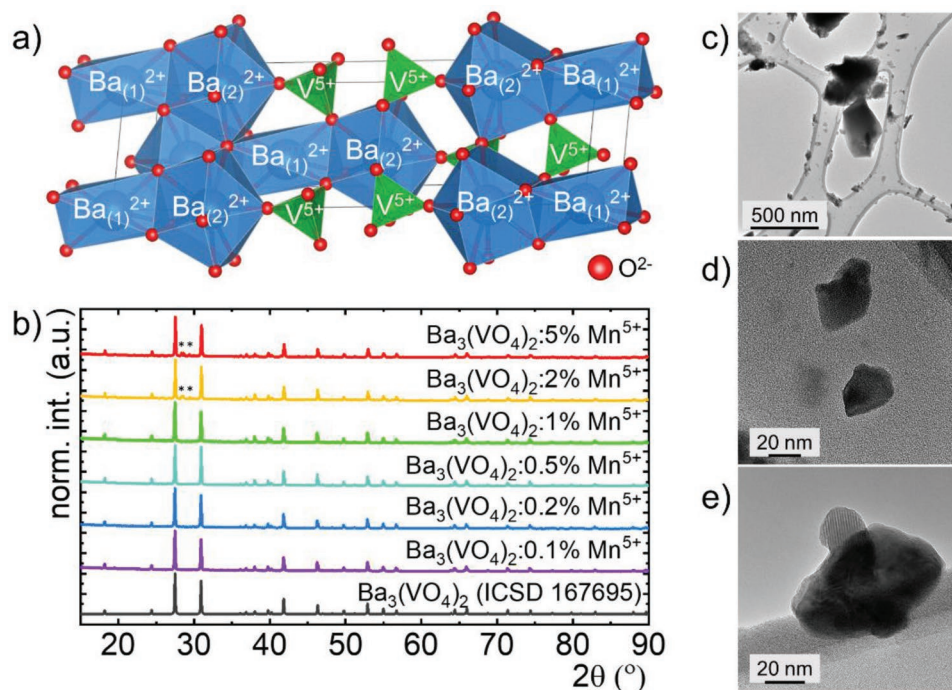
Figure 1. Structural characterization of synthesized materials: a) crystal structure of the $Ba_3(VO_4)_2$ unit cell; b) X-ray diffraction patterns of $Ba_3(VO_4)_2$ doped with different concentrations of Mn^{5+} (reflection of the additional phase marked by asterisk); c–e) the representative TEM images of $Ba_3(VO_4)_2$:0.1% Mn^{5+}, 2% Er^{3+}.

Grzechnik et al.,[39] who additionally mentioned that the substitution of Mn^{5+} ions in V^{5+} sites yields a small distortion of the oxygen tetrahedra surrounding the Mn^{5+} ions and a change in symmetry from C_{3v} to C_s. On the other hand, in the present work, $Ba_3(VO_4)_2$:Mn^{5+} was additionally co-doped with some Ln^{3+} ions, i.e., Pr^{3+}, Nd^{3+}, Er^{3+}, and Tm^{3+}. All the ions considered are known to be located at 8-fold coordinated sites, while the literature did not specify an EIR of these ions in the environment of 10 O^{2-} ions. In this case, the EIRs are 112.6, 110.9, 100.4, and 99.4 pm for 8-fold coordinated Pr^{3+}, Nd^{3+}, Er^{3+}, and Tm^{3+}, respectively, which is ≈40% lower relative to 8-fold coordinated Ba^{2+} ions. In addition, the charge difference should be mentioned in this case.

To verify the phase purity of the synthesized nanocrystals and to investigate the influence of dopant concentration on the crystallographic structure of $Ba_3(VO_4)_2$, their XRPD patterns were analyzed (Figure 1b; also check Figure S1, Supporting Information (ESI) for XRPD patterns in a narrow range of 26–32°). The diffraction reflections obtained for samples doped with Mn^{5+} ions at concentrations from 0.1 to 1% correspond with the reference pattern (ICSD 167695) confirming the phase purity of the synthesized phosphors. For 2 and 5% concentrations of Mn^{5+}, additional diffraction peaks were found at ≈28.35°, 28.60°, and 29.35°, indicating the precipitation of an additional phase. Therefore, these samples were excluded from further analysis. Based on the comparison of the diffraction reflection with the reference patterns from the ICSD database, these peaks can be attributed to $Mn_2V_2O_7$ (ICSD 30687). On the other hand, for high concentrations of Mn^{5+} ions (2% and 5%), a shift of the peaks towards larger angles relative to the reference pattern was observed,

indicating a contraction of the cell size associated with the difference between the ionic radii of V^{5+} and Mn^{5+} ions. This was further confirmed by Rietveld refinement parameters, which are summarized in Table S1 (Supporting Information). The unit cell parameter a of ≈5.791 Å (V = 714.84 Å^3) for 0.1% Mn^{5+} gradually decreased to a value of ≈5.783 Å (V = 712.93 Å^3) for 1% Mn^{5+}. On the other hand, the unit cell parameter c increases slightly with the increase of Mn^{5+} concentration suggesting the parallel expansion of the unit cell toward the z-axis for higher Mn^{5+} content (Figure S2, Supporting Information). Moreover, XRPD patterns obtained for $Ba_3(VO_4)_2$:1% Mn^{5+}, 1% Ln^{3+}, where Ln^{3+} = Pr^{3+}, Nd^{3+}, Er^{3+}, Tm^{3+}, and also $Ba_3(VO_4)_2$:1% Mn^{5+}, x% Er^{3+}, where x = 0.1; 0.2; 0.5; 2 corresponded to the $Ba_3(VO_4)_2$ reference pattern without indicating the occurrence of an additional undesirable crystalline phase (Figures S3 and S4, Supporting Information).

The transmission electron microscopy (TEM) studies of $Ba_3(VO_4)_2$:0.1% Mn^{5+} indicate that well-crystallized particles are prone to agglomeration (Figure 1c–e and Figure S5, Supporting Information). Using Feret's method, the particle size distribution was determined (Figures S6–S8, Supporting Information). More than 90% of the measured particles were found to be less than 100 nm in size, with most particles between 25 and 55 nm. The average particle size for 0.1% Mn^{5+} doped phosphor is estimated to be 52 nm. On the other hand, after analyzing TEM images of $Ba_3(VO_4)_2$:1% Mn^{5+}, 2% Er^{3+}, it can be concluded that co-doping with Ln^{3+} ions even at the highest considered concentration does not lead to significant changes in the size and agglomeration state of crystalline particles (Figures S5–S8, Supporting Information). In this case, the average particle size is ≈72 nm.
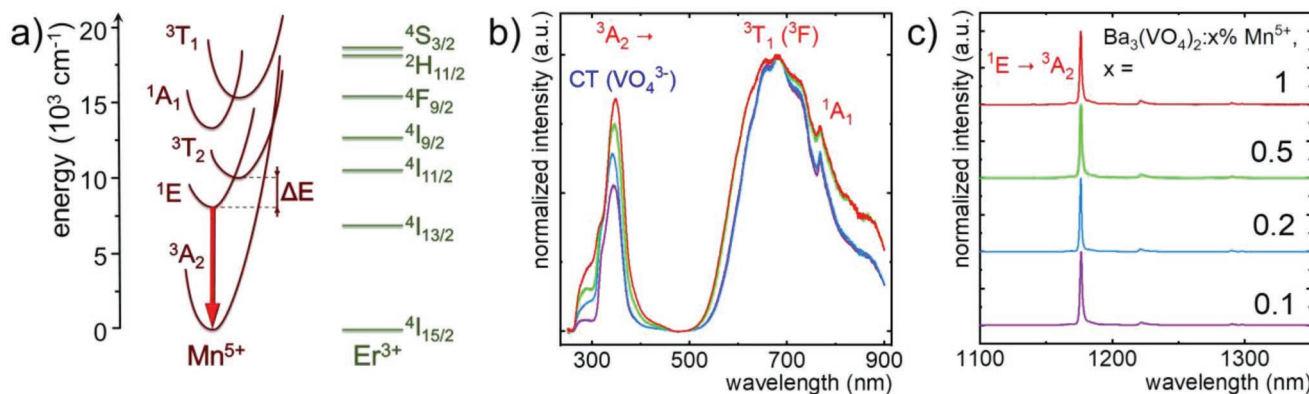
Figure 2.
a) Configurational coordinate diagram for Mn^{5+} and Er^{3+} ions; b) the comparison of low-temperature (83 K) excitation, and c) emission spectra of $Ba_3(VO_4)_2$ doped with different concentrations of Mn^{5+}.

3.2. Luminescent Properties Characterization

The electronic configuration of Mn^{5+} is $3d^2$. However, when the Mn^{5+} ions are located in the tetragonal symmetry the correlation between the energy states of Mn^{5+} ions can be understood by the analysis of the Tanabe-Sugano diagram for $3d^8$ electronic configuration as presented in **Figure 2**a. In this case, the $\lambda_{exc} = 808$ nm excitation wavelength enables the transition of the electrons from the $^3A_2$ ground state to the $^3T_2$ excited state. Subsequently, nonradiative relaxation processes lead to the population of the ^1E state followed by a radiative depopulation resulting in the generation of NIR emission associated with the $^1E{\rightarrow}^3A_2$ electronic transition (the red arrow in Figure 2a). Due to the lack of mutual shift of parabolas $^3A_2$ and ^1E in the wavevector domain, the resulting emission band is expected to be narrow, while the shifted parabola $^3T_2$ will be responsible for activating quenching processes with increasing temperature. These theoretical assumptions are confirmed by the excitation spectra taken at low temperature (83 K) for the $\lambda_{em} = 1178$ nm for $Ba_3(VO_4)_2$:x% Mn^{5+} nanocrystals (Figure 2b). The spectra consist of broad bands with distinctive maxima at 767 nm ($\approx$13040 cm^{-1}), 680 nm ($\approx$14700 cm^{-1}), 346 nm ($\approx$28900 cm^{-1}), and 300 nm ($\approx$33330 cm^{-1}). The first two maxima correspond to the $^3A_2{\rightarrow}^1A_1$ and $^3A_2{\rightarrow}^3T_1(^3F)$ transitions, respectively, while the next two ones in the near ultraviolet (UV) spectral range are associated with a charge transfer transition from the $(VO_4)^{3-}$ group to the Mn^{5+} metal center. Similar bands in the UV spectral range were also observed by Min et al. for undoped $Ba_3(VO_4)_2$ and assigned to the $^1A_2(^1T_1){\rightarrow}^1A_1(^1A_1)$ and $^1A_2(^1T_1){\rightarrow}^1B_2(^1T_2)$ transitions, respectively (see also Figure S9, Supporting Information).[40] A gradual broadening of the excitation bands associated with internal transitions in Mn^{5+} ions with an increase in the dopant concentration can be observed, from a full width at half maximum (FWHM) of $\approx$183 nm for 0.1 and 0.2% Mn^{5+} to $\approx$228 nm for 0.5 and 1% Mn^{5+}. Moreover, after normalizing the excitation spectra to the maximum intensity value located at a wavelength of $\approx$680 nm, an increasing contribution of the $(VO_4)^{3-}$ charge transfer band can be observed with increasing Mn^{5+} ion concentration, suggesting an improvement in the efficiency of energy transfer between the $(VO_4)^{3-}$ group and

Mn^{5+} ions with increasing Mn^{5+} ion concentration. The emission spectra of $Ba_3(VO_4)_2$:Mn^{5+} measured under 808 nm excitation at 83 K consist primarily of an intense narrow band originating from the $^1E{\rightarrow}^3A_2$ transition with a maximum located at 1176.4 $\pm$ 0.3 nm. The FWHM of this band increases slightly with the concentration of Mn^{5+} ions (Figure 2c). As noted by Merkle et al., the band has an asymmetrical shape due to an unresolved doublet of the excited level, which is expected for a small C_{3v} distortion of the oxygen tetrahedron surrounding the Mn^{5+} ions.[36] This is also the reason for the appearance of the vibronic sidebands observed at 1168.1, 1221.4 1290.3, and 1298.1 nm. Furthermore, it should be noted that the emission maximum value differs from the previously reported value of 1181.0 $\pm$ 0.3 nm.[36] This discrepancy is related to the temperature difference at which the measurements were performed, i.e., 83 K and 296 K, respectively. Such a temperature-induced bandshift of Mn^{5+} emission has been previously observed among others for $Sr_3(PO_4)_2$:Mn^{5+} and $Ba_3(PO_4)_2$:Mn^{5+}, and is an effect of the alternation of the integrated intensities of the emission bands associated with electronic transitions between different vibronic levels.[32] In addition, an extremely low FWHM of the emission band was noticed compared to other TM ions. The FWHM for $Ba_3(VO_4)_2$:x% Mn^{5+} with x = 0.1; 0.2; 0.5 and 1% is below 2 nm (from 1.68 $\pm$ 0.3 nm to 1.93 $\pm$ 0.3 nm). The broadening of the emission band may be due to disturbances in the symmetry of crystallographic sites resulting from the substitution of larger V^{5+} ions with slightly smaller Mn^{5+} ions. These phosphors were characterized by relatively high luminescence quantum yield (QY) as for all nanoparticles QY > 20% and the maximal luminescence QY = 51% was found for $Ba_3(VO_4)_2$:1% Mn^{5+}. The high luminescence quantum yield of $Ba_3(VO_4)_2$:1%Mn^{5+} with the high absorption cross-section of the Mn^{5+} ions are very beneficial from the applicative perspective. The analysis of the luminescent decays of ^1E excited state of Mn^{5+} measured at 83 K revealed that the luminescent decays vary significantly with the concentration of Mn^{5+} ions (Figure S10a, Supporting Information). To quantitatively verify the effect of dopant concentration on the lifetime of Mn^{5+} ions, the average lifetimes of the ^1E excited level of Mn^{5+} ions were calculated employing Equation 1:

**ADVANCED
SCIENCE NEWS**

www.advancedsciencenews.com

**ADVANCED
OPTICAL
MATERIALS**

www.advopticalmat.de

$$\tau_{avr} = \frac{A_1 \tau_1^2 + A_2 \tau_2^2}{A_1 \tau_1 + A_2 \tau_2} \quad (1)$$

where: τ_1, τ_2 are the decay parameters and A_1, A_2 are amplitudes of the bi-exponential function:

$$I(t) = I_0 + A_1 \cdot \exp\left(-\frac{t}{\tau_1}\right) + A_2 \cdot \exp\left(-\frac{t}{\tau_2}\right) \quad (2)$$

The values of average lifetimes of Mn^{5+} ions in $Ba_3(VO_4)_2$ are on the order of tenths of milliseconds (Figure S10b, Supporting Information). Significant shortening in lifetimes can be observed for the 0.2% Mn^{5+} sample compared to $\tau_{avr} = 0.381$ ms for $Ba_3(VO_4)_2$:0.1% Mn^{5+} can be observed.

3.3. The Influence of Temperature on the Kinetics of the Luminescence of Mn^{5+} Ions

The kinetics of Mn^{5+} luminescence was analyzed in the 77–703 K temperature range (**Figure 3**a, Figure S11, Supporting Information). Independently of the Mn^{5+} concentration, above 200 K, a very fast thermal shortening of the τ_{avr} can be observed (Figure 3b). However, some differences can be found in the 83–200 K temperature range. In the case of the 0.1% Mn^{5+}, the τ_{avr} in this temperature range remains almost unchanged, whereas for 0.2% Mn^{5+} slight shortening can be observed. On the other hand, in the case of $Ba_3(VO_4)_2$ doped with 0.5% and 1% was observed. Such a thermal elongation of the lifetime was previously reported for Mn^{4+} and Cr^{3+} ions doped phosphors and is usually discussed in terms of relaxation of the selection rules associated with thermally induced mixing of the wavefunctions of excited states.[41,42] Then, between 200 and 500 K, there is a sharp shortening of the excited state lifetimes of Mn^{5+} ions associated with an increase in the probability of the thermal population of electrons from the ^1E level to the $^3T_2$ level, resulting in nonradiative depopulation to the ground level. Therefore, at 503 K, the lifetime reaches 0.054 ms for 0.2% Mn^{5+}. Interestingly, the values obtained of the τ_{avr} are lower compared to those reported for the single-crystal counterpart ($\tau_{avr} = 0.43$ ms at room temperature and even $\tau_{avr} = 1.1$ ms at 11 K).[36] This difference is probably related to the higher probability of nonradiative depopulation of the excited state observed for nanocrystalline phosphors. To quantitatively verify the influence of Mn^{5+} concentration on the thermal changes of the values of τ_{avr}, the relative sensitivity S_R was calculated according to the following formula (Equation 3):
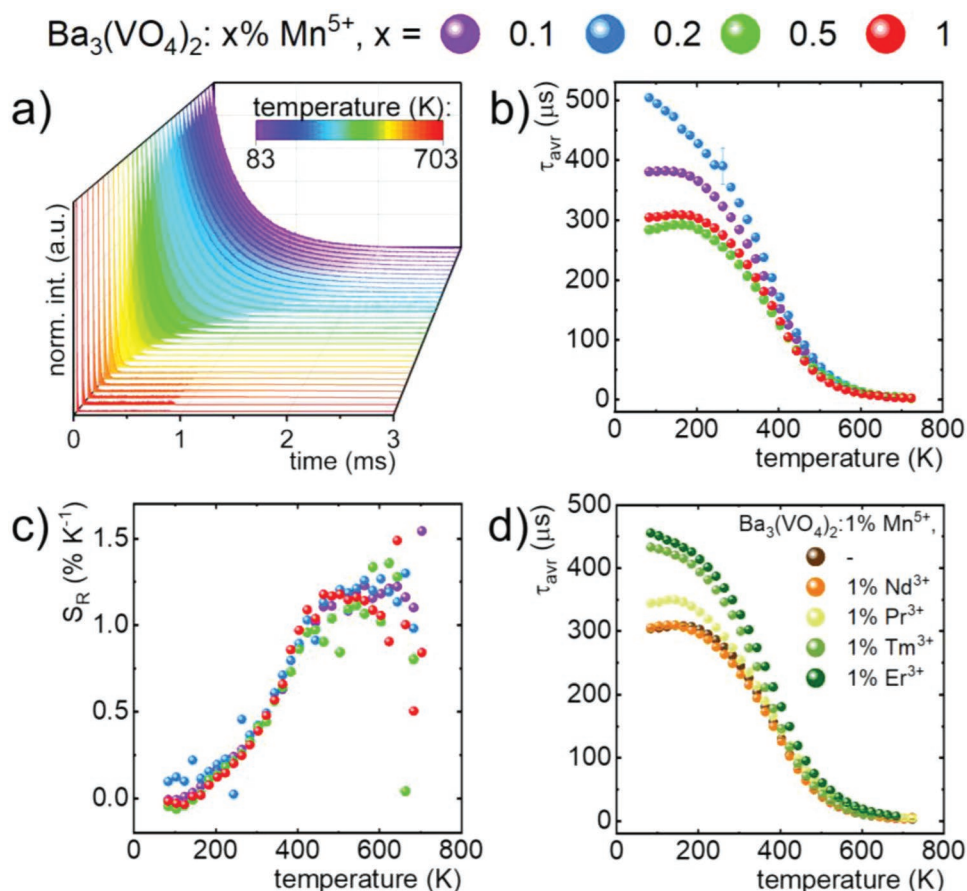
Figure 3. a) Thermal evolution of luminescent decay profiles of emission from ^1E excited state of Mn^{5+} ions for $Ba_3(VO_4)_2$:1% Mn^{5+}; b) thermal evolution of τ_{avr} of Mn^{5+} and c) the S_R for $Ba_3(VO_4)_2$ doped with different Mn^{5+} concentration; d) thermal evolution of τ_{avr} of Mn^{5+} in $Ba_3(VO_4)_2$:1% Mn^{5+} co-doped with 1% Ln^{3+} ions.

$$S_R = \frac{1}{\tau_{avr}} \frac{\Delta\tau_{avr}}{\Delta T} 100\% \tag{3}$$

where and $\Delta\tau_{avr}$ represents the change in τ_{avr} for the ΔT change of temperature. The S_R results plotted in Figure 3c indicate that a small thermal variation in τ_{avr} below 200 K results in $S_R < 0.20\%K^{-1}$. Subsequently, in a wide range of up to 440 K, an increase in sensitivity was observed. For 300 K, very similar values were obtained for all Mn^{5+} doped samples, i.e., in the range from 0.39 (obtained for 1% Mn^{5+}) to 0.42% K^{-1} (obtained for 0.2% Mn^{5+}). At 400 K, larger discrepancies in sensitivity values can be observed from 0.86% K^{-1} (for 0.5% Mn^{5+}) to 0.97%K^{-1} (for 1% Mn^{5+}). It can be seen that the maximum S_{Rmax} values for $Ba_3(VO_4)_2$ doped with Mn^{5+} with concentrations below 0.5% were obtained ≈500 K and maintained between 1.13 and 1.17%K^{-1}. For higher concentrations of Mn^{5+} ions, the S_{Rmax} value was shifted toward lower temperatures, i.e., $S_{Rmax} = 1.17\%$ K^{-1} at 460 K for 1% Mn^{5+}. It should be noted that in the range of 300 – 400 K, the lifetime values, as well as the sensitivities obtained from them, remain at a similar level regardless of the concentration of Mn^{5+} ions. Therefore, due to the highest value of QY and the highest intensity at room temperature, $Ba_3(VO_4)_2$ doped with 1% Mn^{5+} was chosen for further analysis.

In order to improve the relative sensitivity of the thermometer based on the lifetimes of Mn^{5+} ions, it was proposed to use co-doping with Ln^{3+} ions to obtain an additional depopulation channel via thermally activated $Mn^{5+} \rightarrow Ln^{3+}$ energy transfer. Among the Ln^{3+} ions, four representative ions were selected due to the small energy mismatch between the energy levels of Ln^{3+} and Mn^{5+}, which could make them suitable candidates to induce efficient energy transfer, namely Pr^{3+}, Nd^{3+}, $Er^{3+,}$ and Tm^{3+} (Figure S12, Supporting Information). As a result, four samples of $Ba_3(VO_4)_2$ co-doped with 1% Mn^{5+} and 1% Ln^{3+} were synthesized while maintaining the previous synthesis conditions. For the prepared samples, luminescent decays of Mn^{5+} ions were measured as a function of temperature and average excited state lifetimes were calculated (Figure 3d, Figure S13, Supporting Information). Surprisingly, co-doping with all Ln^{3+} ions leads to an increase in the lifetimes of Mn^{5+} ions at 83 K (Figure 3d). The smallest changes, which may be within the margin of error, were observed for $Ba_3(VO_4)_2$:1% Mn^{5+} co-doped with 1% Nd^{3+}, for which $\tau_{avr} = 0.30$ ms was obtained in comparison to $\tau_{avr} = 0.30$ ms at 83 K for the singly-doped counterpart. However, significant changes were noted for nanocrystals with 1% Pr^{3+}, 1% $Tm^{3+,}$ and 1% Er^{3+}, for which the lifetimes of Mn^{5+} ions extended to $\tau_{avr} = 0.34$, 0.43, and even 0.46 ms, respectively. It can be noticed that the co-doping with lanthanide ions of smaller ionic radii (like Tm^{3+} and Er^{3+}) leads to a generation of greater lattice distortion compared to the larger lanthanides (Nd^{3+}, Pr^{3+}). Since the highest extension of lifetimes with co-doping of Ln^{3+}, which greatly facilitates average lifetime determination, was found for Er^{3+} ions, this sample was chosen as the most promising one for thermometric application.

3.4. Influence of Er^{3+} Co-Doping on Mn^{5+} Lifetimes

The elongation of the lifetime of the ^1E state of Mn^{5+} observed in the case of the sample co-doped with Er^{3+} ions is especially beneficial in the context of lifetime-based thermometry for the reasons outlined above. Therefore, this effect was investigated as a function of co-dopant concentration (**Figure 4**a, Figure S14, Supporting Information). The elongation of luminescent decays at low temperature with increasing Er^{3+} ion concentration can be clearly seen (Figure 4b). At 83 K, the lifetimes of Mn^{5+} ions gradually increased as follows: $\tau_{avr} = 0.304$, 0.337, 0.395, 0.458 ms for 0%, 0.1%, 0.2%, and 0.5% of Er^{3+} ions. However, for higher Er^{3+} concentrations, slightly shorter lifetimes were obtained, i.e., $\tau_{avr} = 0.456$ and 0.439 ms for 1% and 2% of Er^{3+}. This effect is probably related to the $Mn^{5+} \rightarrow Er^{3+}$ energy transfer, which is facilitated when the interionic distance is shortened, as is the case for higher Er^{3+} concentrations (confirmed by the observation of the absorption bands of Mn^{5+} ions in the excitation spectra of $Ba_3(VO_4)_2$:1% Mn^{5+}, 1% Er^{3+} measured ate the emission of Er^{3+} ions at 1530 nm, Figure S15, Supporting Information) . A similar dependence on the concentration of Er^{3+} ions is presented by the lifetimes at higher temperatures, but a slightly higher rate of τ_{avr} shortening with increasing temperature is presented by $Ba_3(VO_4)_2$:1% Mn^{5+}, 0.5% Er^{3+}. This is also confirmed by the relative sensitivities calculated from the Mn^{5+} lifetimes (Figure 4c). The S_R values for all Er^{3+} ion concentrations have similar trends versus temperature, but it can be clearly observed that the highest from 83 K to 443 K were obtained for 0.5% Er^{3+}. In this case, $S_R = 0.23\%$ K^{-1}, 0.47% K^{-1} and 1.04% K^{-1} can be mentioned at 203, 303, and 403 K, respectively, with respect to $S_R = 0.11\%$ K^{-1}, 0.39% K^{-1} and 0.93% K^{-1} determined for its singly-doped counterpart at the same temperatures. Moreover, for 0.5% Er^{3+}, there was a shift in S_{Rmax} values toward lower temperatures, i.e., $S_{Rmax} = 1.19\%$ K^{-1} at 443 K with respect to $S_{Rmax} = 1.22\%$ K^{-1} at 483 K obtained equally for 0% and 0.1% Er^{3+}. For samples doped with 0.2%, 1% and 2% of Er^{3+}, S_{Rmax} ranging from 1.08% K^{-1} to 1.11% K^{-1} at 483 or 503 K was achieved. In addition, the temperature determination uncertainty δT was calculated according to Equation S1 (Supporting Information) and is shown in Figure 4d. The δT is a parameter that more precisely assesses the application potential of the tested thermometers because, despite the small differences between the S_R values obtained for different Er^{3+} concentrations, it also considers the lifetime values, which also have a significant impact on the correct temperature readout (determined according to the methodology described in the SI). In the temperature range of 300 – 400 K, δT values not exceeding 0.07 K were obtained for all samples except in the case of the one doped with 2% Er^{3+} ions. At 303 K for singly-doped $Ba_3(VO_4)_2$:1% Mn^{5+}, $\delta T = 0.033$ K was obtained, but this result was improved to $\delta T = 0.026$ K by the sample co-doped with 0.5% of Er^{3+} ions. It is noteworthy that for 1% Mn^{5+}, 0.5% Er^{3+} a value of $\delta T < 0.035$ K was obtained over a wide range from 123 K to 483 K. The δT values obtained in the temperature range of 300 – 400 K, combined with favorable excitation and emission wavelengths located in the NIR-I and NIR-II range, provide high application potential for the studied luminescent thermometers. Therefore, a proof-of-concept experiment for thermal imaging was proposed based on the lifetime of the ^1E state of Mn^{5+} ions through a phantom of tissue-mimicking skin.

The comparison of the thermometric performance of different luminescent thermometers based on the kinetics of the excited state of transition metal ions doped phosphors
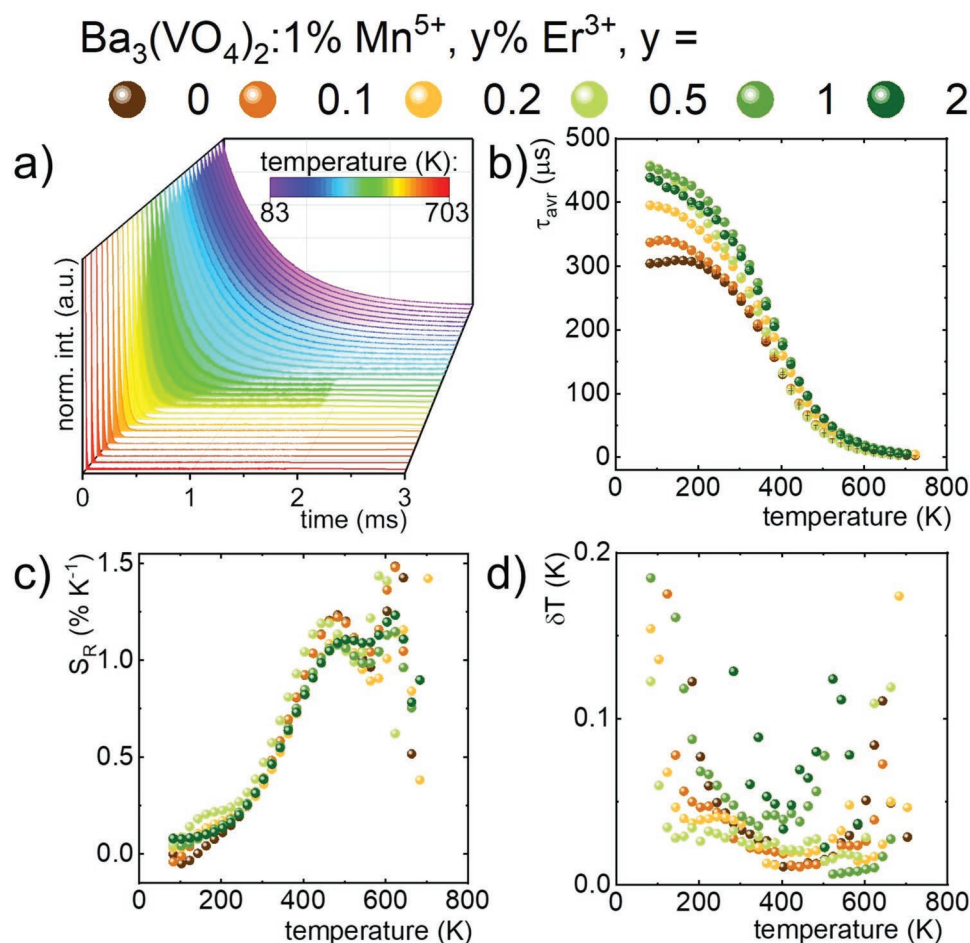
Figure 4. a) Thermal evolution of luminescent decays of ^1E excited state of Mn^{5+} ions for $Ba_3(VO_4)_2$:1% Mn^{5+}, 0.5% Er^{3+}; thermal evolution of b) Mn^{5+} average lifetimes, c) the relative sensitivities and d) temperature uncertainty for $Ba_3(VO_4)_2$:1% Mn^{5+} co-doped with different Er^{3+} concentration.

presented in Table 1 indicates that a higher S_R was found for luminescent thermometers operating in the visible spectral range. In the case of the luminescent thermometers operating in NIR-II, the $Ba_3(VO_4)_2$:Mn^{5+}, Er^{3+} is characterized by relatively high performance and S_R reported, in this case, is slightly higher compared to the $Sr_3(PO_4)_2$:Mn^{5+}.

3.5. Mn^{5+} Lifetime Based Thermal Imaging

To simulate conditions similar to those encountered during the potential use of a luminescence thermometer based on Mn^{5+} ion lifetimes, a tissue phantom was fabricated and its optical properties were optimized to mimic the ones of skin (see

Table 1. Comparison of spectroscopic parameters of representative thermometers based on the luminescent lifetime of transition metal ions.

| Host	Emitting state	S_R [%/K]	$T(S_{RMAX})$ [K]	λ_{exc} [nm]	λ_{em} [nm]	Operating temperature range [K]	Ref.
$Sr_3(PO_4)_2$:Mn^{5+}	^1E	1.00	443	668	1173	123-573	[32]
$Ca_2Al_2SiO_7$:Cr^{4+}	$^3T_1$	0.25	300	730	1230	293-353	[43]
$MgTiO_3$:Mn^{4+}	^2E	4.1	277	550	697	198-323	[44]
$Li_4Ti_5O_{12}$:Mn^{4+}	^2E	2.6	330	500	696	10-350	[45]
Mg_2TiO_4:Cr^{3+}	^2E	0.75	290	473	700	100-400	[46]
$YAlO_3$:Cr^{3+}	^2E	0.58	302	445	688	123-573	[47]
$LiGa_5O_8$:Cr^{3+}	^2E	0.76	295	406	≈720	298-563	[48]
$SrTiO_3$:Mn^{4+}, Er^{3+}	^2E	5.1	290	400	725	77-450	[49]
$SrTiO_3$:Ti^{3+}, Tb^{3+}	^2E	8.83	180	400	791	77-240	[50]
$Ba_3(VO_4)_2$:Mn^{4+}, Er^{3+}	^1E	1.19	443	808	1181	350-500	This work

details in Equations S1-S8, Figures S16–S20, Table S2, Supporting Information). The promising results in temperature sensing based on the kinetics of the luminescence of Mn^{5+} ions in $Ba_3(VO_4)_2$: Mn^{5+}, Er^{3+} motivated the implementation of this material for thermal imaging. Therefore the proof-of-concept experiment of thermal imaging using $Ba_3(VO_4)_2$:1% Mn^{5+}, 0.5% Er^{3+} nanocrystals was designed as shown in **Figure 5**a,b. The phosphor was located between two glass slides and placed with one of the shorter edges on a heating plate and the other on an ice pack to obtain a temperature gradient. Two sets of experiments were performed, namely with and without a layer of 2.6-mm thick tissue phantom with 50% intralipids and 0.1% Indian ink placed on top of the glass plate (hence along both the excitation and emission optical paths), completely covering the area where the luminescent material was located. In the first step, for the two systems tested without and with tissue phantom, a series of measurements were made at a fixed temperature, set with the heating plate and monitored with the thermal camera (Figure S19, Supporting Information for representative maps). From these, average lifetimes were calculated from average intensities and tabulated as a function of temperature in the form of a calibration curve (Figure S20, Supporting Information). The resulting lifetimes for the phosphor covered by tissue phantom in the range ≈298–306 K are slightly shorter by ≈5 µs than the non-covered counterpart. However, above 306 K the values of the error bars of the lifetimes obtained with tissue phantom (2-3 µs) are in the limit of the values determined without tissue phantom. Due to the low values of the error bars (≈0.8 µs), it was decided to use the temperature dependence of the lifetimes determined for the sample without tissue phantom as a calibration curve (described by the Mott-Seitz model, see also Supporting Information). Based on the calibration curve determined from the experimental setup for thermal imaging, the relative sensitivity was determined, which, due to the small temperature range, ranges from S_R = 0.68 to 0.72% K^{-1} in the 300–320 K range and temperature determination uncertainty below δT = 0.017 K (Figure S21, Supporting Information). Subsequently, the temperature on the heating plate was set to 340 K to obtain a temperature gradient throughout the glass slide (Figure 5c). A single measurement lasted ≈30 seconds and the temperature readout during this time varied by an error of ±0.1 K at the two controlled points (at the "cold" and "hot" edges). Due to the intrinsic nature of the infrared thermal camera, which measures the temperature of the first surface encountered, the detected temperature of the tissue phantom was ≈3.5 K lower than that of the glass slide under the same experimental conditions (Figure 5d). The phosphor was excited with a single square-wave pulse from a λ_{exc} = 808 nm laser diode. The NIR camera was synchronized and triggered at a precisely defined delay time to the excitation laser and allowing it to attain the series of luminescence images with decreasing intensity with a delay between images equal to 5 µs. A fitting script based on the bi-exponential equation (Equation 2) was then applied to the series of images to obtain lifetime maps (Figure 5e,f). The range of obtained lifetimes as a function of distance from the heating plate varied from τ_{avr} = ≈220 µs to ≈280 µs. In the lifetime maps made through tissue phantom, noisier images were obtained. Using the previously received calibration curve, the

Mott-Seitz equation (Equation S8, Supporting Information) was used for fitting. On this basis, it was possible to transpose the lifetime maps shown in Figure 5e,f to the thermal maps using two color scales. In addition, in order to quantitatively compare the results obtained from the temperature map with thermal camera images, 2D line profiles at the center of the shorter edge of the specimen, shown by dashed lines in Figures 5c–f), were selected and juxtaposed as temperature plots as a function of distance from the heating plate (Figure 5g,h). Comparing the two graphs, it can be observed that the thermal camera temperature curve for the sample with tissue phantom starts from a lower temperature, i.e., ≈338 K with respect to ≈340 K for the sample without phantom, as well as the temperature of the point furthest away from heating is higher: 301 K with respect to 299 K. This confirms that the thermal camera is able to read the temperature of the first encountered surface, i.e., the tissue phantom, which, although it also reflects the temperature gradient well (as might be expected given its relatively small thickness of 2.6 mm), the marginal values of the gradient differ from those read for the phosphor without tissue phantom. A very similar thermal trend was obtained across the analyzed sample using Mn^{5+} lifetime in the experiments with and without tissue phantom. This is probably due to the significant effect of signal scattering leading to the luminescent material and also emitted through the tissue phantom. Therefore, it should be concluded that it may be convenient to use several points that could be averaged to ensure a correct temperature readout, and this could be realized with a NIR camera having a better resolution. Nevertheless, with this experiment, we were able to confirm the functionality of the $Ba_3(VO_4)_2$:Mn^{5+}, Er^{3+} phosphor for temperature imaging based on lifetimes, as well as the effectiveness of using this method in studies for thermal sensing through tissue. All the experiments presented clearly confirm the high application potential of $Ba_3(VO_4)_2$:Mn^{5+}, Er^{3+} for thermal imaging. Additionally, the NIR-to-NIR operating range, high luminescence quantum yield, and high absorption cross-section of Mn^{5+} in the NIR-I are key features particularly relevant from the perspective of in vivo applications. Therefore $Ba_3(VO_4)_2$:Mn^{5+}, Er^{3+} is a very promising temperature probe of high applicative potential.

4. Conclusion

We have herein reported a Mn^{5+}-based $Ba_3(VO_4)_2$ nanophosphor optimized to perform as an efficient lifetime-based luminescent thermometer. Structural, morphological, and spectroscopic studies highlighted how strong Mn^{5+} near-infrared emission ($^1E \rightarrow {}^3A_2$ transition centred within 1150–1200 nm) with long luminescence lifetime (>200 µs around room temperature) can be attained by fine-tuning the concentration of the transition metal and co-doping with controlled amounts of Er^{3+}. The optimized composition of the nanothermometer is $Ba_3(VO_4)_2$:1% Mn^{5+}, 0.5% Er^{3+}, which, under the tested conditions, features a relative thermal sensitivity between 0.5 and 1.2% K^{-1} and an associated uncertainty consistently <0.1 K in the 350–500 K temperature range.

We then tested the prowess of the developed luminescent nanothermometer for thermal sensing in close-to-real-life

2202366 (9 of 12)
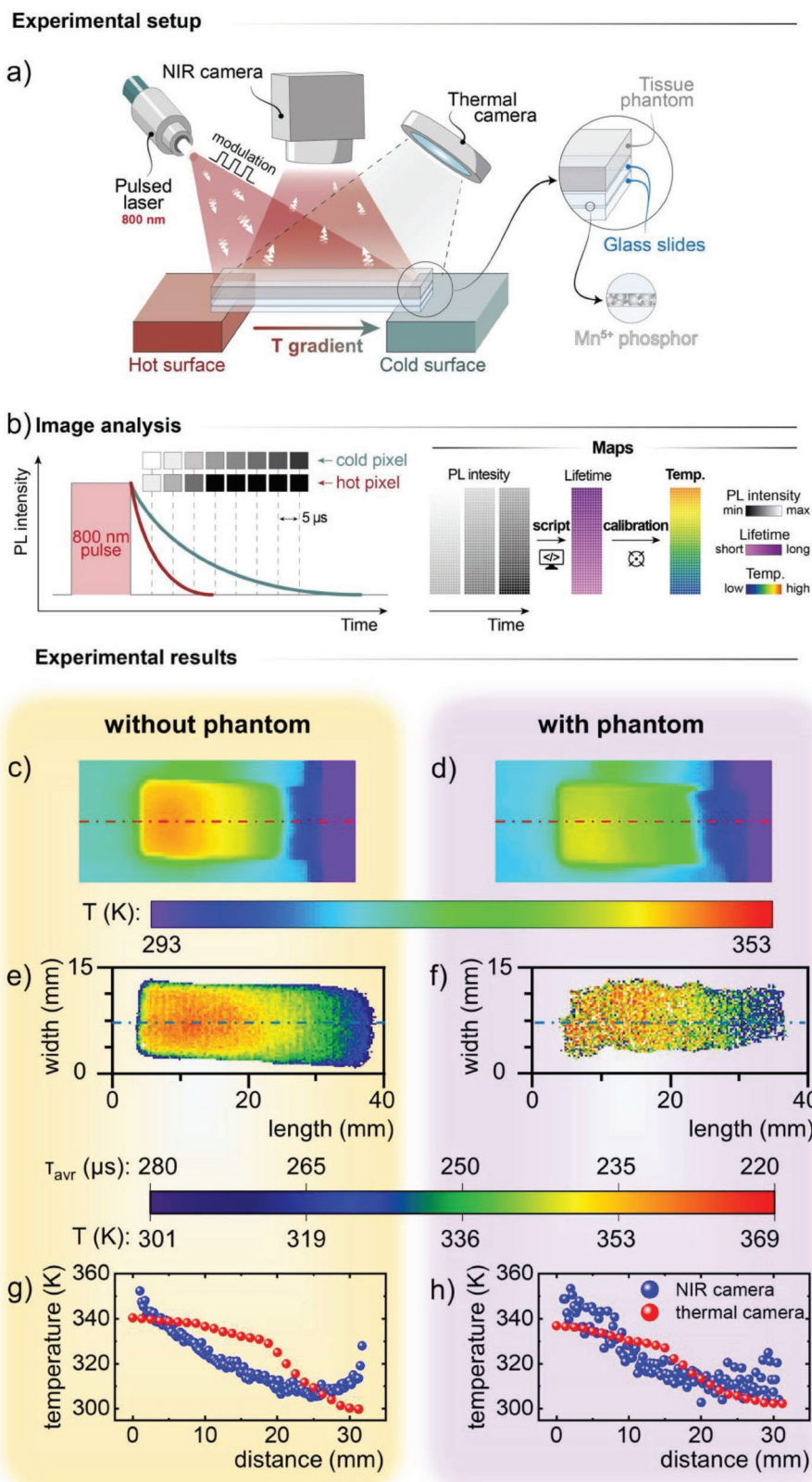
Figure 5. a) Schematic visualization of the proof-of-concept experiment of thermal imaging using $Ba_3(VO_4)_2$:1% Mn^{5+}, 0.5% Er^{3+} nanocrystals; b) the obtained images analysis procedure; c,d) the representative thermal images of the system without (c) and with (d) tissue phantom; and e,f) corresponding images obtained based on the kinetics of the ^1E state of Mn^{5+} ions; g,h) the comparison of the thermal profiles across the blue lines in (e) and (f) obtained using thermal camera (red points) and luminescence thermometry (blue dots) for the sample without (g) and with (h) tissue phantom.

2202366 (10 of 12)

conditions. We specifically demonstrated that 2D temperature maps of a thermal gradient can be obtained through tissue phantoms mimicking the optical properties of the skin using $Ba_3(VO_4)_2$:1% Mn^{5+}, 0.5% Er^{3+} nanophosphors as luminescent probes and a custom-made setup for lifetime-based luminescence thermometry.

These results show the way for the development of ever more efficient luminescent nanothermometers based on doped luminescent centers (i.e., metal ions) that are bright and feature long, temperature-dependent lifetimes. The possibility to remotely and reliably monitor thermal gradients through 2.6 mm of tissue phantom further supports the recent trends in luminescence thermometry of shifting toward lifetime-based approaches, owing to their robustness and higher accuracy.

Supporting Information

Supporting Information is available from the Wiley Online Library or from the author.

Conflict of Interest

The authors declare no conflict of interest.

Data Availability Statement

The data that support the findings of this study are available on request from the corresponding author. The data are not publicly available due to privacy or ethical restrictions.

[1] M. Tan, F. Li, N. Cao, H. Li, X. Wang, C. Zhang, D. Jaque, G. Chen, *Small* **2020**, *16*, 2004118.

[2] J. Morales-Dalmau, C. Vilches, I. de Miguel, V. Sanz, R. Quidant, *Nanoscale* **2018**, *10*, 2632.

[3] Y. Liu, K. Ai, J. Liu, M. Deng, Y. He, L. Lu, *Adv. Mater.* **2013**, *25*, 1353.

[4] S. Jain, D. G. Hirst, J. M. O'Sullivan, *Br. J. Radiol.* **2012**, *85*, 1010.

[5] R. Taylor, S. Coulombe, T. Otanicar, P. Phelan, A. Gunawan, W. Lv, G. Rosengarten, R. Prasher, H. Tyagi, *J. Appl. Phys.* **2013**, *113*, 011301.

[6] A. Espinosa, R. Di Corato, J. Kolosnjaj-Tabi, P. Flaud, T. Pellegrino, C. Wilhelm, *ACS Nano* **2016**, *10*, 2436.

[7] C. D. S. Brites, S. Balabhadra, L. D. Carlos, *Adv. Opt. Mater.* **2019**, *7*, 1801239.

[8] C. D. S. Brites, A. Millán, L. D. Carlos, *In Handbook on the Physics and Chemistry of Rare Earths* (Eds.: B. Jean-Claude, K. Vitalij), Elsevier, **2016**, pp. 339.

[9] A. Lozano, F. Hassanipour, *Infrared Phys. Technol.* **2019**, *97*, 244.

[10] K. Trejgis, A. Bednarkiewicz, L. Marciniak, *Nanoscale* **2020**, *12*, 4667.

[11] L. Labrador-Páez, M. Pedroni, A. Speghini, J. García-Solé, P. Haro-González, D. Jaque, *Nanoscale* **2018**, *10*, 22319.

[12] B. del Rosal, E. Ximendes, U. Rocha, D. Jaque, *Adv. Opt. Mater.* **2017**, *5*, 1600508.

[13] Y. Shen, J. Lifante, N. Fernández, D. Jaque, E. Ximendes, *ACS Nano* **2020**, *14*, 4122.

[14] A. Bednarkiewicz, J. Drabik, K. Trejgis, D. Jaque, E. Ximendes, L. Marciniak, *Appl. Phys. Rev.* **2021**, *8*, 011317.

[15] G. Liu, Z. Sun, Z. Fu, L. Ma, X. Wang, *Talanta* **2017**, *169*, 181.

[16] M. Suta, Ž. Antić, V. Đorđević, S. Kuzman, M. D. Dramićanin, A. Meijerink, *Making Nd3+ a sensitive luminescent thermometer for physiological temperatures—an account of pitfalls in boltzmann thermometry*, Vol. *10*, **2020**.

[17] M. Kong, Y. Gu, Y. Chai, J. Ke, Y. Liu, X. Xu, Z. Li, W. Feng, F. Li, *Sci. China Chem.* **2021**, *64*, 974.

[18] H. D. A. Santos, E. C. Ximendes, M. del C Iglesias-de la Cruz, I. Chaves-Coira, B. del Rosal, C. Jacinto, L. Monge, I. Rubia-Rodríguez, D. Ortega, S. Mateos, J. GarcíaSolé, D. Jaque, N. Fernández, *Adv. Funct. Mater.* **2018**, *28*, 1803924.

[19] E. Ximendes, A. Benayas, D. Jaque, R. Marin, *ACS Nano* **2021**, *15*, 1917.

[20] R. Bhargava, B. J. Davis, *presented at Proc. SPIE*, **2009**.

[21] Y.-H. Ong, Y. Zhu, T. C. Zhu, *presented at Proc. SPIE*, **2019**.

[22] S. L. Jacques, *Phys. Med. Biol.* **2013**, *58*, R37.

[23] J. R. Casar, C. A. McLellan, C. Siefe, J. A. Dionne, *ACS Photonics* **2021**, *8*, 3.

[24] A. Bednarkiewicz, L. Marciniak, L. D. Carlos, D. Jaque, *Nanoscale* **2020**, *12*, 14405.

[25] Y. Shen, J. Lifante, I. Zabala-Gutierrez, M. de la Fuente-Fernández, M. Granado, N. Fernández, J. Rubio-Retama, D. Jaque, R. Marin, E. Ximendes, A. Benayas, *Adv. Mater.* **2022**, *34*, 2107764.

[26] W. Becker, *J. Microsc.* **2012**, *247*, 119.

[27] K. Y. Zhang, Q. Yu, H. Wei, S. Liu, Q. Zhao, W. Huang, *Chem. Rev.* **2018**, *118*, 1770.

[28] Y. Wu, J. Y. Qu, *J. Biomed. Opt.* **2006**, *11*, 054023.

[29] L. Marciniak, K. Kniec, K. Elżbieciak-Piecka, K. Trejgis, J. Stefanska, M. Dramićanin, *Coord. Chem. Rev.* **2022**, *469*, 214671.

[30] M. G. Brik, C.-G. Ma, *Theoretical Spectroscopy of Transition Metal and Rare Earth Ions*, **2019**.

[31] H. H. Kung, *Review of Spectroscopy of Transition Metal Ions on Surfaces*, Vol. *213*, Leuven University Press, Belgium **2001**.

[32] Z. Ristić, W. Piotrowski, M. Medić, J. Periša, Ž. M. Antić, L. Marciniak, M. D. Dramićanin, *ACS Appl. Electron. Mater.* **2022**, *4*, 1057.

[33] M. D. Dramićanin, Ł. Marciniak, S. Kuzman, W. Piotrowski, Z. Ristić, J. Periša, I. Evans, J. Mitrić, V. Đorđević, N. Romčević, M. G. Brik, C.-G. Ma, *Light Sci. Appl.* **2022**, *11*, 279.

[34] P. M. Gschwend, D. Niedbalka, L. R. H. Gerken, I. K. Herrmann, S. E. Pratsinis, *Adv. Sci.* **2020**, *7*, 2000370.

[35] R. D. Shannon, *Acta Crystallogr., Sect. A: Found. Crystallogr.* **1976**, *32*, 751.

[36] L. D. Merkle, A. Pinto, H. R. Verdún, B. McIntosh, *Appl. Phys. Lett.* **1992**, *61*, 2386.

**ADVANCED
SCIENCE NEWS**

www.advancedsciencenews.com

**ADVANCED
OPTICAL
MATERIALS**

www.advopticalmat.de

[37] M. P. Pechini, *US3330697A*, **1967**.

[38] J. Yao, T. Muñoz-Ortiz, F. Sanz-Rodríguez, E. Martín Rodríguez, D. H. Ortgies, J. García Solé, D. Jaque, R. Marin, *ACS Photonics* **2022**, *9*, 559.

[39] A. Grzechnik, P. F. McMillan, *J. Solid State Chem.* **1997**, *132*, 156.

[40] W. Piotrowski, L. Dalipi, K. Elzbieciak-Piecka, A. Bednarkiewicz, B. Fond, L. Marciniak, *Adv. Photonics Res.* **2022**, *3*, 2100139.

[41] M. Back, J. Ueda, M. G. Brik, T. Lesniewski, M. Grinberg, S. Tanabe, *ACS Appl. Mater. Interfaces* **2018**, *10*, 41512.

[42] M. Grinberg, T. Lesniewski, S. Mahlik, R. S. Liu, *Opt. Mater.* **2017**, *74*, 93.

[43] X. Chen, S. Liu, K. Huang, J. Nie, R. Kang, X. Tian, S. Zhang, Y. Li, J. Qiu, *Chem. Eng. J.* **2020**, *396*, 125201.

[44] E. Glais, V. Dordević, J. Papan, B. Viana, M. D. Dramićanin, *RSC Adv.* **2018**, *8*, 18341.

[45] M. Medić, Z. Ristić, S. Kuzman, V. Đorđević, I. Vukoje, M. G. Brik, M. D. Dramićanin, *J. Lumin.* **2020**, *228*, 117646.

[46] Z. Ristić, V. Đorđević, M. Medić, S. Kuzman, M. G. Brik, Ž. Antić, M. D. Dramićanin, *Opt. Mater.* **2021**, *120*, 111468.

[47] K. Elzbieciak-Piecka, J. Drabik, D. Jaque, L. Marciniak, *Phys. Chem. Chem. Phys.* **2020**, *22*, 25949.

[48] D. Chen, Z. Wan, Y. Zhou, Z. Ji, *J. Eur. Ceram. Soc.* **2015**, *35*, 4211.

[49] W. M. Piotrowski, K. Trejgis, M. Dramicanin, L. Marciniak, *J. Mater. Chem. C* **2021**, *9*, 10309.

[50] W. Piotrowski, M. Kuchowicz, M. Dramićanin, L. Marciniak, *Chem. Eng. J.* **2022**, *428*, 131165.